

Power-Efficient Actuation for Insect-Scale Autonomous Underwater Vehicles

Cody R. Longwell, Conor K. Trygstad, and Néstor O. Pérez-Arancibia

Washington State University, Pullman, WA 99164-2920, USA

cody.longwell@wsu.edu, conor.trygstad@wsu.edu, n.perezarancibia@wsu.edu

Abstract. We present a new evolution of the *Very Little Eel-Inspired roBot*, the VLEIBot⁺⁺, a 900-mg swimmer propelled by two 10-mg bare *high-work-density* (HWD) actuators driven by *shape-memory alloy* (SMA) wires. An actuator of this type consumes an average power of about 40 mW during in-air operation. We integrated onboard power and computation by using a custom-built *printed circuit board* (PCB) and an 11-mAh 3.7-V 507-mg single-cell *lithium-ion* (Li-Ion) battery, which in conjunction enable autonomous swimming for about 20 min on a single charge. The VLEIBot⁺⁺ can swim at speeds of up to 18.7 mm/s (0.46 Bl/s) and is the first subgram microswimmer with onboard power, actuation, and computation developed to date. Unfortunately, the approach employed to actuate this robot is infeasible for underwater applications because a typical 10-mg bare SMA-based actuator requires an average power of approximately 800 mW when operating underwater. To address this issue, we introduce a new 13-mg power-efficient SMA-based actuator that can function with similar power requirements (~ 80 mW on average) and output performance (~ 3 mm at low frequencies) in air and water. This design uses a sealed flexible air-capsule to enclose the SMA wires that drive the actuator and thus passively control the heat-transfer rate of the thermal system. Furthermore, this new power-efficient encapsulated actuator requires low voltages of excitation (3 to 4 V) and simple power electronics to function. The breakthroughs presented in this paper represent a path towards the creation of insect-scale *autonomous underwater vehicles* (AUVs).

Keywords: Micro/Nano Robots, Actuation, Aquatic Robotics

1 An Aquatic Frontier for Microrobotics

The recent introduction of new microfabrication methods, actuation materials, propulsion mechanisms, and control approaches for microrobotics has enabled the development of several novel high-performance aquatic [1–4], aerial [5–7], and terrestrial [8–11] insect-scale robots. We envision a future in which swarms of triphibious microrobots work in coordination with humans to assist in search and rescue operations, pollution detection and mitigation, infrastructure and facility inspections, and automated pest control, just to mention a few possibilities. For this vision to become a reality, the deployed microrobots must

C. R. Longwell and C. K. Trygstad contributed equally to this research.

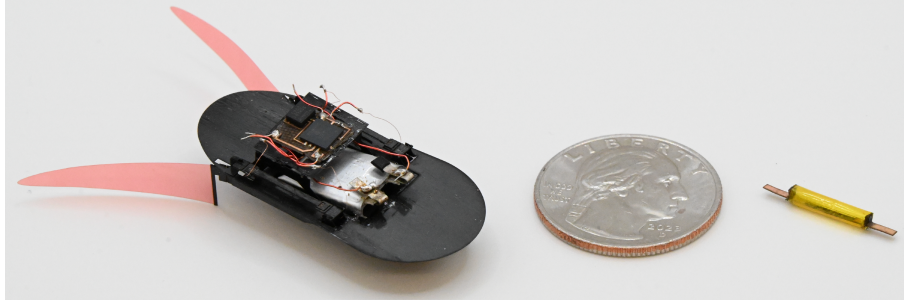


Fig. 1. A swimmer and an actuator. The VLEIBot⁺⁺ (*left*), a 900-mg autonomous surface swimmer driven by two 10-mg bare SMA-based actuators; and, a new low-power 13-mg encapsulated HWD SMA-based actuator for underwater operation (*right*). This new actuator has a length of 15.25 mm, a volume without the capsule of 2.37 mm³, and a volume with the capsule of 33.02 mm³. The actuators that drive the VLEIBot⁺⁺ have a length of 12 mm and volume of 1.89 mm³ each.

operate autonomously in unstructured fields and adapt to environmental uncertainties. Currently, the majority of microrobotic platforms either function physically tethered to power sources [1–12] or rely on large and complex external actuation apparatuses that are impractical for use in real-life situations [13–15]. While the creation of novel actuation and energy-storage technologies has contributed to the realization of new mm-to-cm-scale autonomous terrestrial vehicles [16–19], these technologies have not yet been leveraged to develop insect-sized *autonomous underwater vehicles* (AUVs). On the other hand, a significant number of cm-to-dm-scale underwater vehicles showing great promise for deployment in unstructured fields have been produced in the past two decades [20–28]; however, all these platforms use actuation methods and power sources that are not easily scalable to mm-to-cm sizes.

One approach that has been successfully demonstrated to be mm-scalable is microactuation based on the use of tensioned thin *shape-memory alloy* (SMA) wires [10, 11]. Theoretically, SMA-based microactuation is a promising path towards the development of insect-scale AUVs because it exhibits *high work densities* (HWDs), requires low excitation voltages, is passively controllable using simple structures made of *carbon fiber* (CF), and can be driven with simple battery-excitable power electronics. Using this technology, we created the VLEIBot⁺⁺, the 900-mg autonomous surface swimmer shown in Fig. 1. This microrobot is an evolution of the swimmers presented in [2] and is driven by 10-mg low-power bare SMA-based actuators designed to operate in air. During swimming, an onboard 11-mAh 3.7-V 507-mg single-cell *lithium-ion* (Li-Ion) battery and a custom-built *printed circuit board* (PCB) provide power for onboard computation and actuation. The VLEIBot⁺⁺ is the first subgram autonomous surface microrobotic swimmer developed to date and can achieve locomotion speeds of up to 18.7 mm/s (0.46 Bl/s). We believe that these results represent a breakthrough in microrobotics because it is well known that swimming using traditional human-scale methods becomes increasingly difficult as the Reynolds number decreases [29]. Each bare SMA-based microactuator employed to drive

the VLEIBot⁺⁺ consumes an average power of approximately 40 mW only, thus enabling about 20 min of operational time on a single battery charge. Unfortunately, this swimmer is currently constrained to function on the surface of water to keep its actuators dry while swimming, as their power efficiency is significantly degraded when excited underwater. Specifically, when operating underwater, these devices require an average power on the order of 800 mW, which represents an increase of about 1900% with respect to the in-air actuation case. These figures indicate that the development of a VLEIBot⁺⁺-like underwater swimmer electrically driven by bare SMA-based microactuators is infeasible due to the low energy and power densities of even the most advanced batteries currently available. The problem at the core of this issue is that the heat-transfer coefficient of water is significantly larger than that of air at normal conditions of temperature and pressure (20 °C; 1 atm). To address this challenge, we introduce a new 13-mg low-power SMA-based actuator—shown in Fig. 1—which is capable of both in-air and underwater operation with almost identical power requirements; namely, about 80 mW, on average, during actuation in both media. This measurement represents an improvement of about 90% in energy efficiency with respect to that obtained with a bare SMA-based actuator functioning in water. As seen in Fig. 1, in the proposed design, the SMA wires that drive the actuator are encapsulated using a Kapton-made flexible chamber that passively controls the local rate of heat transfer. This innovation opens a new technological path towards the realization of lightweight low-power actuation for insect-scale AUVs.

The rest of the paper is organized as follows. Section 2 describes the design and fabrication of the VLEIBot⁺⁺, and discusses preliminary untethered swimming experiments. Section 3 presents experimental results regarding the power-consumption characterization of a 10-mg bare SMA-based actuator, and describes the proposed 13-mg low-power SMA-based actuator, which is capable of power-efficient underwater operation. Last, Section 4 summarizes the findings produced through the presented research and states future directions for the development of insect-scale AUVs.

2 The VLEIBot⁺⁺: An Autonomous Subgram Swimmer

2.1 Design and Fabrication of the VLEIBot⁺⁺

The design and procedure used to fabricate a VLEIBot⁺⁺ prototype are shown in Fig. 2. The main element that enables tetherless SMA-based actuation for this swimmer is the custom-built PCB depicted in Figs. 2(a) and (b). As seen in Fig. 2(a), the PCB is fabricated in three steps. In Step 1, sheets of *copper-clad FR4* (CuFR4) are laser etched to remove areas of the Cu-coating and thus create the patterns designed for each side of the PCB. In Step 2, the two sides of the PCB are pin-aligned and adhered together with a sheet of Pyralux adhesive by applying pressure and heat inside a curing oven. In Step 3, the off-the-shelf elements composing the interconnected power, actuation, and computation circuits are installed on the two sides of the PCB using conductive silver epoxy (MG-Chemicals 8331D) and cured inside an oven. Schematics of the two sides of the fabricated PCB are shown in Fig. 2(b). The top side of the PCB includes a *micro controller unit* (MCU)—Microchip

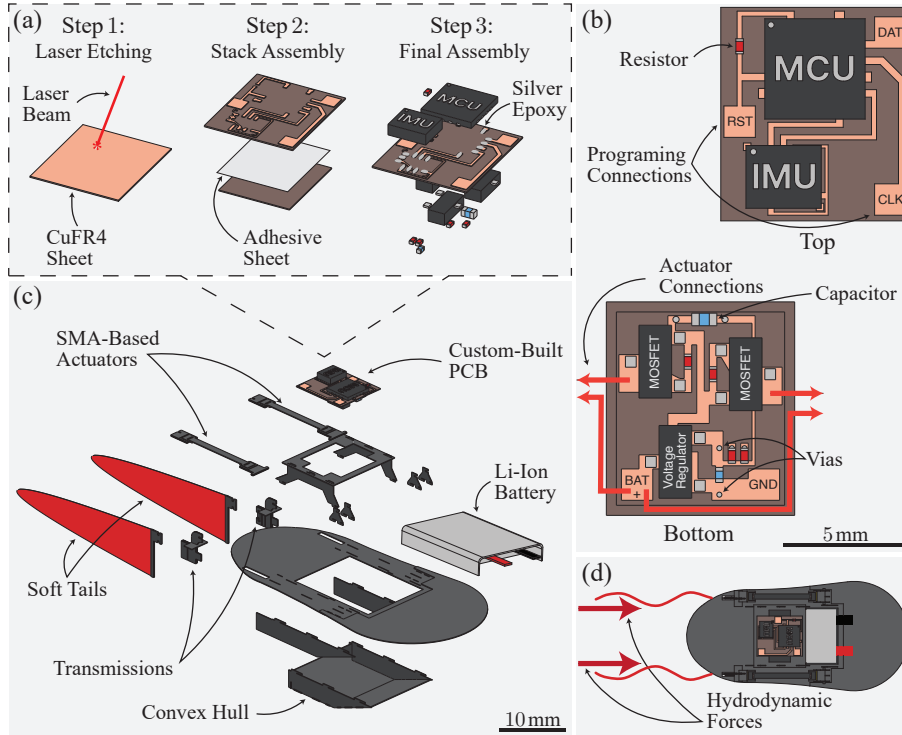


Fig. 2. Design and fabrication of the VLEIBot⁺⁺. (a) Fabrication process of the robot's custom-designed PCB. In Step 1, sheets of CuFR4 are etched using laser rasterization in order to remove areas of the Cu-coating and thus create the patterns designed for each side of the PCB. In Step 2, the two sides of the PCB are pin-aligned and adhered together with a sheet of Pyralux adhesive by applying pressure and heat inside a curing oven. In Step 3, the off-the-shelf elements composing the interconnected power, actuation, and computation circuits are installed on the two sides of the PCB using conductive silver epoxy (MG-Chemicals 8331D) and cured inside an oven. (b) Top and bottom of the robot's PCB. The top side of the PCB supports an MCU for computation and an IMU for sensing. The bottom side of the PCB supports two N-channel MOSFETs and a voltage regulator. The two sides of the PCB are connected through *vias*. Decoupling capacitors and pull-up/down resistors are necessary to ensure the functionality of the circuits. (c) Exploded view of the VLEIBot⁺⁺'s design. This robot is composed of six main types of components: (i) two bare SMA-based microactuators of the type described in [2] with passive hinges installed at their ends; (ii) two soft propulsors that propel the microswimmer forward; (iii) two transmissions that amplify the output displacements generated by the robot's actuators into the two significantly larger stroke angles required to excite the two soft propulsors of the swimmer; (iv) a convex hull made of CF that provides a buoyancy force to support the microswimmer on water; (v) an 11-mAh 3.7-V 507-mg single-cell Li-Ion battery (Powerstream GM301014H); and, (vi) the custom-built PCB described in (a). (d) Swimming mode of the VLEIBot⁺⁺. The two bare SMA-based microactuators undulate the tails of the swimmer to produce the hydrodynamic forces required for forward propulsion.

Technology PIC16F18326-I/JQ—and an *inertial measurement unit* (IMU)—STMicroelectronics LSM6DSOXTR—which respectively perform onboard computation and sensing. We included programming ports to the circuit design, which are required to upload the operational C-code that runs the MCU; the programming is implemented using an MPLabs PicKit 4 in-circuit debugger tool and the MPLabs X IDE v6.20 developer environment. The bottom side of the PCB includes two *metal-oxide-semiconductor field-effect transistors* (MOS-FETs), which function as switches that open and close the current-flow pathways to the SMA actuators when triggered by *pulse-width modulation* (PWM) signals generated by the MCU. As seen in Fig. 2(b), the bottom side of the PCB also includes a regulator that stabilizes the voltage delivered by the Li-Ion battery to power the MCU and IMU. The two sides of the PCB are connected to each other through cylindrical *vias* filled with conductive silver epoxy. Also, decoupling capacitors and pull-up/down resistors were included in the PCB design to ensure proper circuit functionality.

The assembly of a VLEIBot⁺⁺ prototype is graphically described in Fig. 2(c). This robot consists of six main types of components: (i) two bare SMA-based microactuators of the type described in [2] that drive the propulsors of the swimmer; (ii) two soft tails that generate the hydrodynamic forces required for locomotion through *fluid-structure interaction* (FSI); (iii) two planar four-bar linkage transmissions that amplify the displacement outputs of the actuators into large stroke angles that undulate the two soft tails of the swimmer; (iv) a convex hull made of CF that provides a container to store the system’s battery and generates a buoyancy force that works in parallel with the surface tension of water to maintain the swimmer afloat; (v) an 11-mAh 3.7-V 507-mg single-cell Li-Ion battery (Powerstream GM301014H) that enables the swimmer to operate continuously and autonomously for about 20 min; and, (vi) the custom-built PCB illustrated in Figs. 2(a) and (b). To complete the assembly procedure, all the components of the prototype are connected together and secured using *cyanoacrylate* (CA) glue (Loctite 414) and the swimmer’s hull is sealed by lining the inside and outside of all the structure’s seams with CA glue. The SMA wires that drive the actuators are made of nitinol with a nominal transition temperature of 90 °C and diameter of 0.0381 mm (Dynalloy 90 °C HT). A schematic that explains the basic swimming mode of the VLEIBot⁺⁺ is shown in Fig. 2(d). As discussed in [2], when the two soft tails of the propulsors are flapped, the resulting undulations produce through FSI the hydrodynamic forces that propel the swimmer forward. By independently modulating the two PWM signals that excite the two propulsors of the swimmer, we can vary the magnitude and direction of the total thrust propelling the system. As a result, *two-dimensional* (2D) controllability is achieved, as empirically demonstrated through the feedback-controlled swimming tests performed using the VLEIBot⁺ presented in [2].

2.2 Swimming Experiments of the VLEIBot⁺⁺

To assess and demonstrate the functionality, basic controllability, and performance of a 900-mg VLEIBot⁺⁺ prototype during autonomous operation, we conducted feedforward-controlled swimming tests. Fig. 3 presents experimental data from three tests in which the swimmer was programmed to excite its

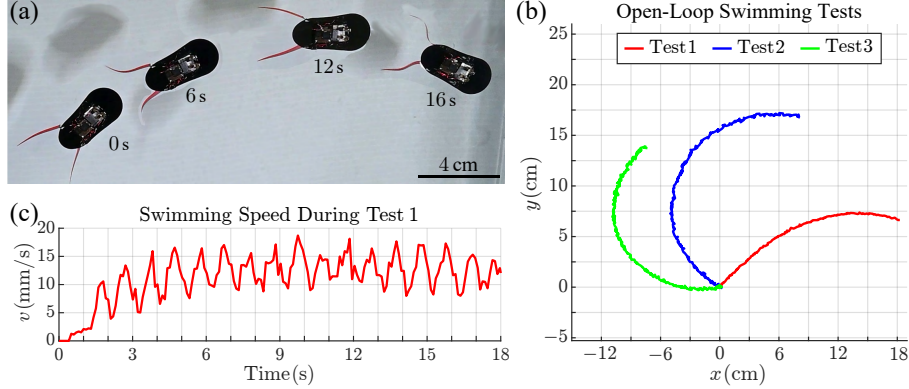


Fig. 3. Open-loop swimming experiments of the VLEIBot⁺⁺. (a) Photographic composite of frames taken at 6-s intervals from video footage of open-loop swimming Test 1. (b) 2D trajectories of the VLEIBot⁺⁺, $\{x, y\}$, during open-loop swimming Tests 1, 2, and 3. In this plot, we placed the beginning of the trajectories at $\{0, 0\}$ for the purpose of comparison. (c) Swimming speed, v , during Test 1. In this test, we measured average and maximum speeds of 11.9 mm/s and 18.7 mm/s, respectively. Video footage of these swimming experiments can be seen in the accompanying supplementary movie. This movie is also available at <https://wsuamsl.com/resources/ISRR2024movie.mp4>.

bare SMA-based microactuators using PWM signals with a frequency of 1 Hz and *duty cycle* (DC) of 5%. Here, Fig. 3(a) shows a photographic composite of frames taken at intervals of 6 s from overhead footage of Test 1. We estimated the trajectories of the tested prototype during swimming, through frame-by-frame video analyses, using a custom-programmed Matlab script. The trajectories of the swimmer during the three performed open-loop tests are shown in Fig. 3(b). Here, it can be observed that the swimmer repeatedly turned right in the three presented experiments, which indicates an inherent right-hand bias most likely produced by minor fabrication errors. From these simple tests, we conclude that for the VLEIBot⁺⁺ to stably follow trajectories in the 2D space, feedback control methods, such as those introduced in [2], must be implemented. Additionally, we believe that turning biases can be eliminated by improving the propulsors' consistency of fabrication, a matter of current and further research in our laboratory. An important characteristic of any AUV—regardless of its size—is its agility, which is determined by the maximum achievable locomotion speed and turning rates. To estimate the VLEIBot⁺⁺'s forward speed, v , from the experimental data, we used a discrete-time derivative algorithm and a one-second moving-average digital filter. Fig. 3(c) shows the swimmer's speed throughout Test 1; in this case, we measured an average speed of 11.9 mm/s (0.29 Bl/s) and a maximum speed of 18.7 mm/s (0.46 Bl/s). The observed swimming functionality and measured performance of the tested prototype are very preliminary but highly promising. Overall, the VLEIBot⁺⁺ represents a significant step towards the creation of insect-scale AUVs in terms of propulsion, actuation, control, and computation. One major technical challenge that we still must overcome in order to develop a fully functional insect-scale AUV is efficient low-power underwater microactuation. We address this issue in the next section.

3 A New 13-mg Low-Power Underwater Actuator

Most actuators based on the thermal excitation of SMAs exhibit highly dissimilar behaviors in air and water due to the significantly different heat-transfer coefficients of these two media. Specifically, while the bare SMA-based microactuators that drive the VLEIBot⁺⁺ can function efficiently with the power electronics and energy-storage methods discussed in Section 2 when operated in air, no SMA-based microactuator capable of functioning efficiently underwater has been developed to this date. In this section, we present experimental data regarding the power consumption of a typical bare 10-mg SMA-based microactuator of the type used to drive VLEIBot⁺⁺ prototypes, state the identified challenges that need to be addressed to create low-power underwater SMA-based microactuation, and present design predictions empirically tested through the development of a new 13-mg power-efficient SMA-based microactuator for underwater operation conceived to drive insect-scale AUVs.

3.1 Bare SMA-Based Microactuator During Underwater Operation

To measure the power consumed by the tested 10-mg bare SMA-based microactuator while operating in both air and water, we used the experimental setup illustrated in Fig. 4(a). In this setup, a Mathworks Simulink Real-Time host–target system, equipped with a National Instruments PCI-6229 *analog-digital/digital-analog* (AD/DA) board, is employed to generate the PWM signal that triggers the MOSFET-based circuit (four-channel YNMOS-4) that excites the tested actuator through tether wires, according to the same method presented in [2]. During the tests, we utilize an intensity sensor (Adafruit INA260 in conjunction with an Arduino UNO) and a laser displacement sensor (Keyence LK-031) to measure the instantaneous current that flows through the SMA wire that drives the actuator and resulting instantaneous actuation output, respectively. With the purpose of measuring the device’s power consumption accurately, we minimize the power dissipated through the tether wires by using five 52-AWG conductors in parallel. This configuration provides an energy-efficient electrical connection that is sufficiently flexible not to affect actuation performance. Following the *ceteris paribus* principle, in order to physically ensure the same actuation response in air and water, we supply the tested device with an *on*-height voltage—specifically, 2.7 V in air and 12 V in water—that nominally produces the same low-frequency displacement output (~ 3 mm) during a PWM cycle in both media. Through simple experiments, we determined that using a laser sensor to measure displacement through acrylic and water produces an attenuated measurement. To correct this issue, we empirically identified a static mapping between the *perturbed* displacement measurement, d_p —sensed through acrylic and water as seen in Fig. 4(a)—and the *true* displacement, d_t —sensed through air. For the particular setup used in the experiments presented here, we determined that $d_t = 1.58 \cdot d_p$.

We computed the instantaneous electrical power, P , consumed by the tested bare SMA-based actuator using the measured current and resistance of the NiTi SMA wire (Dynalloy 90 °C HT, with a diameter of 0.0381 mm), whose value we determined empirically together with that of the tether wires ($\sim 12 \Omega$). As seen in Figs. 4(b) and (c), we computed the power consumption, in air and water, for

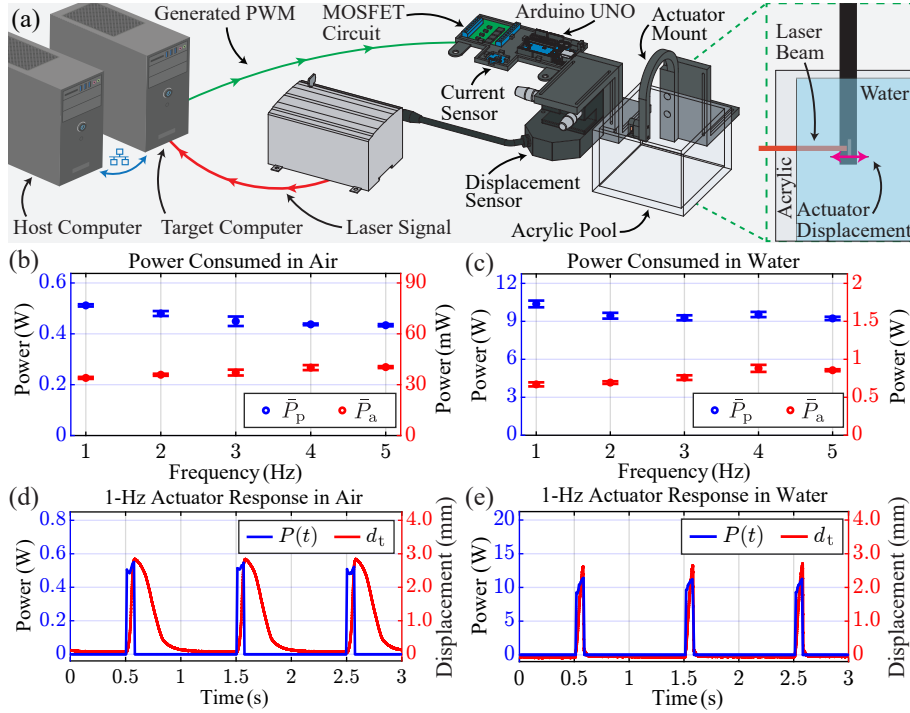


Fig. 4. Power-consumption characterization of bare SMA-based actuator.

(a) Experimental setup used in the characterization experiments. A Mathworks Simulink Real-Time host-target system, equipped with a National Instruments PCI-6229 AD/DA board, is used to generate the PWM signal that triggers the MOSFET-based circuit (four-channel YNMOS-4) that excites the tested actuator; a current sensor (Adafruit INA260 in conjunction with an Arduino UNO) measures and records the current that flows through the SMA wire that drives the actuator; a laser displacement sensor (Keyence LK-031) measures the instantaneous actuation output and the corresponding data are recorded using the host-target system at a sampling rate of 5 kHz. We performed the in-air characterization first; then, we performed the underwater characterization using an acrylic pool filled with water. In (b) and (c), respectively corresponding to operation in air and water, each blue data point indicates the mean of five P_p values, \bar{P}_p , and associated ESD corresponding to five back-to-back experiments, for the five different PWM pairs, $\{f, DC\}$, considered here; and, each red data point indicates the mean of five P_a values, \bar{P}_a , and associated ESD corresponding to the same five back-to-back experiments. Operating in air at $f = 1$ Hz and $DC = 7\%$, we measured average and peak power consumptions on the orders of 40 mW and 0.5 W, respectively. Operating underwater at $f = 1$ Hz and $DC = 7\%$, we measured average and peak power consumptions on the orders of 800 mW and 10.6 W, respectively. (d)–(e) Show, in red, the responses of the actuator to a 1-Hz 7-percent PWM voltage while operating in air and water, respectively; and, in blue, the corresponding instantaneous power consumptions. Video footage of the tested bare SMA-based actuator operating in both air and water can be viewed in the accompanying supplementary movie. This movie is also available at <https://wsuamsl.com/resources/ISRR2024movie.mp4>.

five different PWM excitations; namely, those defined by the frequency-DC pairs, $\{f, \text{DC}\}$, in the matching sets $f \in \{1, 2, 3, 4, 5\}$ Hz and $\text{DC} \in \{7, 8, 9, 10, 10\}\%$. For each test, we computed the peak power, P_p , by averaging all the maximum values of P —which coincide with the times at which the exciting PWM signal is in the *on*-state—over a steady-state period of 30 s; similarly, we obtained the average power, P_a , by computing the mean of P over a steady-state period of 30 s. In Figs. 4(b) and (c), each blue data point indicates the mean of five P_p values, \bar{P}_p , and associated *experimental standard deviation* (ESD) corresponding to five back-to-back experiments, for the five different PWM pairs, $\{f, \text{DC}\}$, considered here; and, each red data point indicates the mean of five P_a values, \bar{P}_a , and associated ESD corresponding to the same five back-to-back experiments. For in-air operation, \bar{P}_p is on the order of 0.5 W at a PWM frequency of 1 Hz and slightly decreases as the frequency increases; \bar{P}_a is on the order of 40 mW for frequencies above 3 Hz and slightly less at lower frequencies. For underwater operation, \bar{P}_p is on the order of 10 W at a PWM frequency of 1 Hz and slightly decreases as the frequency increases; \bar{P}_a is on the order of 800 mW for frequencies greater than 3 Hz and slightly less at lower frequencies. This increase of about 1900 % in average power consumption clearly indicates that the bare SMA-based microactuators developed to drive VLEIBot⁺⁺ prototypes do not represent a feasible possibility for insect-scale AUVs because large amounts of energy would need to be carried onboard to sustain reasonably long mission times. These findings prompted us to address the problem of underwater power consumption in SMA-based microactuation. We propose and discuss a solution next.

3.2 A New Low-Power Underwater SMA-Based Microactuator

From simple observation of the actuator responses presented in Figs. 4(d) and (e), we can conclude that during underwater operation, the tested bare SMA-based actuator rapidly returns to its rest position when the exciting PWM signal transitions from the *on*-state to the *off*-state. Assuming that the stress experienced by the SMA wire that drives a microactuator is similar in air and water, the noticeably faster actuation responses to excitation variations during underwater operation compared to those occurred in air—observed in Fig. 4(e)—are explained by the substantially more rapid cooling of the SMA material in water than in air. This phenomenon occurs because the heat-transfer coefficient of water is significantly larger than that of air at normal conditions of temperature and pressure (20 °C; 1 atm). This observation suggests that power-efficient underwater SMA-based microactuation can be achieved by reducing the heat-transfer coefficient of the local media surrounding the SMA wire driving the system to a level similar to that of air at 20 °C. Here, we use fundamental heat-transfer analyses to assess the feasibility of a design with the potential to achieve low-power actuation in water, which we discuss next.

Heat-Transfer Analysis. We use a lumped model to describe the heat-transfer dynamics of a generic piece of material [30]. Namely,

$$\frac{dT}{dt} = \frac{1}{mC_p} (Q_{\text{in}} - Q_{\text{out}}), \quad (1)$$

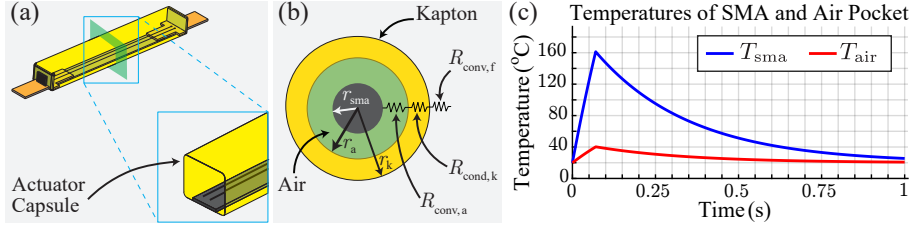


Fig. 5. Proposed solution for underwater actuation. (a) Design of encapsulated SMA-based microactuator capable of underwater operation. (b) One-dimensional heat-transfer model of an SMA wire surrounded by an air pocket contained by a Kapton-made capsule. $R_{cond,k}$ is the thermal resistance for conduction through the Kapton membrane, $R_{conv,a}$ and $R_{conv,f}$ are the thermal resistances for convection through the air and external fluid (air or water), respectively. (c) Numerical-simulation results for the temperatures over time of both the driving SMA wire, T_{sma} , and air cavity, T_{air} , during a 1-Hz 7-percent PWM-excited actuation cycle of the encapsulated microactuator during underwater operation.

in which T is the temperature of the material; m is the mass of the piece; C_p is the specific heat capacity of the material; Q_{in} is the rate at which heat is transferred into the piece; and, Q_{out} is the rate at which heat is transferred out of the piece, estimated as

$$Q_{out} = \frac{T_h - T_c}{R_{eq}}, \quad (2)$$

in which T_h and T_c are respectively the hotter and colder temperatures of the two points at the edges of the equivalent thermal resistance R_{eq} ; and, $R_{eq} = R_{conv} + R_{cond}$, where R_{conv} and R_{cond} are lumped convection and conduction thermal resistances, respectively. Using the notion of thermal resistance network for cylindrical tubes [30], in the case considered here,

$$R_{cond} = \frac{\ln(r_{in}/r_{out})}{2\pi Lk} \quad \text{and} \quad R_{conv} = \frac{1}{\bar{h}A_c}, \quad (3)$$

where r_{in} is the inner radius of the modeled tube; r_{out} is the outer radius of the tube; L is the length of the tube; k is the thermal conductivity of the material; \bar{h} is the estimated heat-transfer coefficient between the material and surrounding environment; and, A_c is the contact area through which heat is transferred.

The value of \bar{h} depends on both the properties of the surrounding fluid and kinematics of the corresponding flow. For gases, typical values are in the range of 2 to 250 W/(m² · K); for liquids, typical values are in the range of 50 to 20000 W/(m² · K) [30]. This significant difference between the heat-transfer coefficients in air and water is the reason behind the considerable increase in power consumption when the tested bare SMA-based actuator is operated underwater. To address this problem, we present the design-based solution depicted in Fig. 5. This design is based on the use of an insulating capsule made of a thin layer of Kapton (7.5 μm) that contains air, as depicted in Fig. 5(a). The insulating pocket of air significantly reduces the local heat-transfer coefficient of the

media surrounding the SMA wire. The membrane of Kapton serves as an impermeable barrier that prevents leaking and also offers low resistance to heat transfer, which keeps the air in the capsule at a temperature close to that of the surrounding water. To assess its feasibility, we use the idealization shown in Fig. 5(b). As seen, we assume an encapsulated SMA wire with an annular air pocket enclosed by a Kapton membrane, in which $r_{\text{sma}} = 0.01905$ mm is the radius of the modeled bare SMA wire; $r_{\text{a}} - r_{\text{sma}} = 0.1$ mm is the annular thickness of the air pocket; $r_{\text{k}} - (r_{\text{a}} + r_{\text{sma}}) = 0.0127$ mm is the thickness of the Kapton membrane; $R_{\text{conv,a}}$ is the thermal resistance across the air pocket; $R_{\text{cond,k}}$ is the thermal resistance across the Kapton membrane; and, $R_{\text{conv,f}}$ is the thermal resistance from the Kapton membrane's surface to the surrounding fluid.

The temperature dynamics of both the SMA wire and annular air pocket can be described using the model specified by (1). In this case, the average rate at which heat is transferred into the SMA material through Joule heating during a PWM-excited actuation cycle is $Q_{\text{in,sma}} = 10^{-2} \cdot \text{DC} \cdot R_{\text{sma}} \cdot I^2$, where $R_{\text{sma}} = 8.9 \Omega$ and $I = 125$ mA are the electrical resistance of the SMA wire and current flowing through it during the *on*-section of the exciting PWM cycle, respectively. In this analysis, we assume a PWM signal with a frequency of 1 Hz and DC of 7%. Next, to estimate $R_{\text{conv,a}}$, we use the convection equation in (3) with a heat-transfer coefficient of $210 \text{ W}/(\text{m}^2 \cdot \text{K})$ and wire length of 10 mm. To estimate $R_{\text{conv,f}}$, we assume the same length of 10 mm and a heat-transfer coefficient in water of $5000 \text{ W}/(\text{m}^2 \cdot \text{K})$. To estimate $R_{\text{cond,k}}$, we use the conduction equation in (3), assuming a wire length of 10 mm and a thermal conductivity of $0.2 \text{ W}/(\text{m} \cdot \text{K})$. According to the modeling approach depicted in Fig. 5(b), heat is first transferred from the SMA material into the air pocket; then, heat is transferred through the Kapton membrane into the surrounding water. Fig. 5(c) shows the simulated temperature evolution of both the SMA material and air pocket over one PWM cycle, assuming that the actuator is immersed in water with a temperature of 20°C . These simulations were implemented in Matlab using a discretized version of (1) with a step size of 10^{-8} s. To simulate the temperature of the SMA material, we used a mass of $7.35 \cdot 10^{-8}$ kg and specific heat capacity of $836.8 \text{ J}/(\text{kg} \cdot \text{K})$; to simulate the temperature of the annular air pocket, we used a mass of $5.31 \cdot 10^{-10}$ kg and specific heat capacity of $1005 \text{ J}/(\text{kg} \cdot \text{K})$. Here, it can be seen that the piece of NiTi SMA material (Dynalloy 90°C HT, with a diameter of 0.0381 mm) surpasses its nominal transition temperature while the temperature of the air cavity remains relatively close to that of the surrounding water (20°C). These results indicate that by using a sealed capsule filled with air to provide a local medium for the SMA wires driving the microactuator, we can achieve levels of power consumption similar to those measured during the characterization experiments of the tested bare SMA-based microactuator operating in air, while achieving similar mechanical functionality.

Design and Fabrication of Microactuator for Underwater Operation.

The fabrication process of the proposed low-power encapsulated SMA-based microactuator is depicted in Fig. 6. As seen, actuators are fabricated in sets of four and the procedure consists of four steps. In Step 1, the SMA wires (Dynalloy 90°C HT; 0.038 mm) and CF beams composing the actuators are installed on

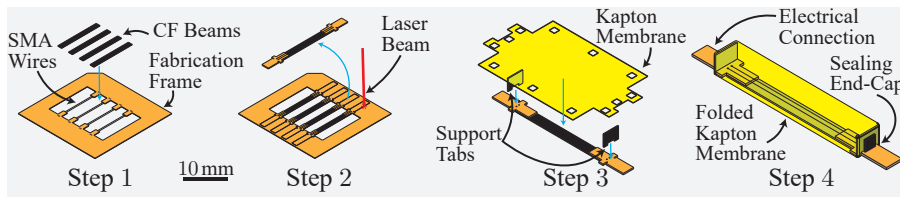


Fig. 6. Fabrication of SMA-based encapsulated actuator. In Step 1, NiTi SMA wires (Dynalloy 90 °C HT; 0.038 mm) and CF beams are installed on a precut fabrication frame. In Step 2, a 355-nm 3-W laser (Photonics Industries DCH-355-3) is used to release the assembled actuators with integrated electrical-connection tabs. In Step 3, for each bare actuator fabricated in Step 2, CF support tabs are attached to the device’s structure, and a foldable sheet made of Kapton is perforated and patterned using the high-power laser. In Step 4, for each actuator, the precut Kapton membrane is folded over the support tabs and the CF beam; to seal the ends of the resulting capsule, CF end-caps are installed and fixed using CA glue. The seam of the Kapton capsule is folded over the CF beam and sealed using flexible silicone adhesive (Smooth-On Sil-Poxy).

a fabrication frame according to the process described in [10]. In Step 2, the four actuators with their electrical connections are cut from the fabrication frame using a high-power laser (Photonics Industries DHC-355-3). In Step 3, CF support tabs are attached to the bare actuators fabricated in Step 2, and foldable sheets made of Kapton are perforated and patterned using the high-power laser. In Step 4, for each actuator, a precut Kapton membrane is folded over the support tabs and the CF beam; to seal the ends of the resulting capsule, CF end-caps are installed and fixed using CA glue. After the Kapton membrane is folded around the CF beam, the seam of the capsule is sealed using flexible silicone adhesive (Smooth-On Sil-Poxy) to prevent leaking during actuation. Cu-FR4 tabs cut from the fabrication frame in Step 2 allow electrical connection to the SMA wires through the Kapton membrane. After testing the functionality of the actuator in air, the electrical connections are sealed using a coating of CA glue (Loctite 414) before underwater testing. After fabrication, the proposed encapsulated SMA-based microactuator weighs only 13 mg, a 30% increase from the original bare SMA-based actuator; we tested its functionality and performance in both air and water, and measured its power consumption in both media through a series of experiments that we discuss next.

Power Characterization of Proposed 13-mg Encapsulated Actuator.

To characterize the power consumption of the proposed 13-mg encapsulated SMA-based actuator in both air and water, we used the experimental setup already described in Section 3.1; however, we replaced the Adafruit INA260 current sensor with a Pololu 05AU measuring device, whose outputted voltage was read directly using the AD/DA board of the setup. As in the power characterization of the bare SMA-based actuator presented in Section 3.1, we electrically connected the tested encapsulated actuator to its two ends using five 52-AWG wires in parallel. Through empirical observations, we determined that an *on*-height excitation voltage of 3.3 V induces the tested encapsulated actuator to generate output displacements comparable to those generated by the

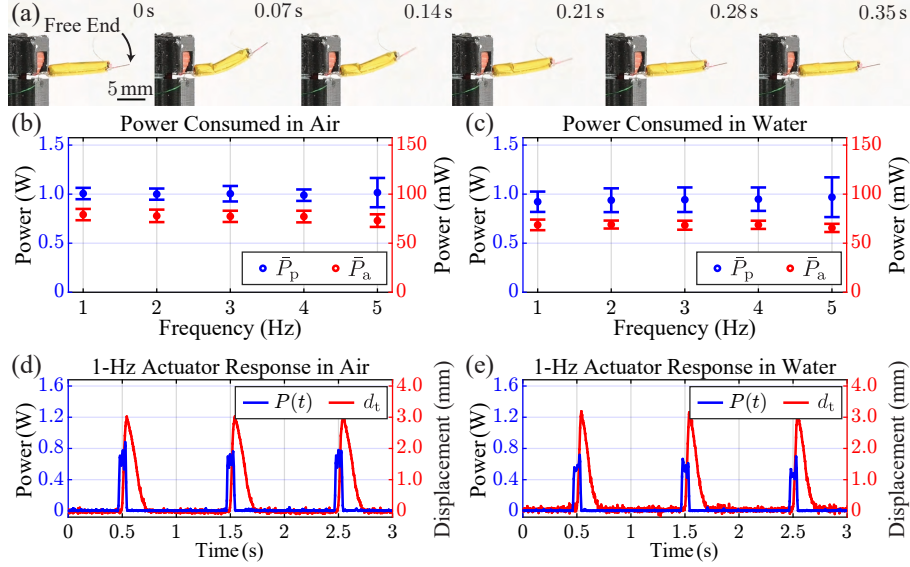


Fig. 7. Power-consumption characterization of encapsulated SMA-based actuator. During characterization, the tested device was excited using the PWM signals defined by the pairs $\{f, DC\}$ in the matching sets $f \in \{1, 2, 3, 4, 5\}$ Hz and $DC \in \{7, 8, 9, 10, 10\}\%$, with an *on*-height of 3.3 V. (a) Photographic sequence, taken from lateral video footage, of one actuation cycle of the tested encapsulated microactuator operating underwater at 1 Hz. In (b) and (c), respectively corresponding to operation in air and water, each blue data point indicates the mean of five P_p values, \bar{P}_p , and associated ESD corresponding to five back-to-back experiments, for the five different PWM pairs, $\{f, DC\}$, considered here; and, each red data point indicates the mean of five P_a values, \bar{P}_a , and associated ESD corresponding to the same five back-to-back experiments. Operating in air at $f = 1$ Hz and $DC = 7\%$, we measured average and peak power consumptions on the orders of 80 mW and 1 W, respectively. Operating underwater at $f = 1$ Hz and $DC = 7\%$, we measured average and peak power consumptions on the orders of 70 mW and 0.97 W, respectively. (d)–(e) Show, in red, responses of the actuator to a 1-Hz 7-percent PWM voltage while operating in air and water, respectively; and, in blue, the corresponding instantaneous power consumptions. Video footage of the proposed encapsulated SMA-based actuator operating in both air and water can be viewed in the accompanying supplementary movie. This movie is also available at <https://wsuamsl.com/resources/ISRR2024movie.mp4>.

tested bare SMA-based actuator (see Section 3.1). The experimental data obtained from testing an encapsulated prototype are summarized in Fig. 7. Here, Fig. 7(a) shows a photographic sequence, taken from lateral video footage, of one actuation cycle of the tested device operating underwater and excited by a PWM signal with a frequency of 1 Hz, DC of 7%, and *on*-height voltage of 3.3 V. In Figs. 7(b) and (c), respectively corresponding to operation in air and water, each blue data point indicates the mean of five P_p values, \bar{P}_p , and associated ESD corresponding to five back-to-back experiments, for the five different PWM pairs, $\{f, DC\}$, considered here; and, each red data point indicates the mean of five P_a values, \bar{P}_a , and associated ESD corresponding to the same five back-to-back

experiments. Figs. 7(d) and (e) present, in red, the actuator responses, d_t , excited by a PWM signal with a frequency of 1 Hz, DC of 7%, and *on*-height voltage of 3.3 V, during operation in air and water, respectively; estimates of the corresponding instantaneous consumed electrical powers are shown in blue. As seen, we measured average and peak power consumptions at 1 Hz on the orders of 80 mW and 1 W, respectively. As expected by design, we measured a similar power consumption when operating underwater; namely, average and peak power consumptions at 1 Hz on the orders of 70 mW and 0.97 W, respectively. While the in-air average power consumption at 1 Hz, relative to that measured for the tested bare actuator, increases from about 40 mW to about 80 mW—an increase of approximately 100%—the underwater average power consumption decreases from about 800 mW to about 70 mW—a drastic decrease of approximately 91%. These results constitute the main contribution of this paper.

4 Conclusions and Future Directions

We presented a new 900-mg surface swimmer, the VLEIBot⁺⁺, which employs two low-power bare SMA-based microactuators—in conjunction with a lightweight custom-built PCB that provides sensing, computation, and electronic capabilities—to locomote autonomously. A single charge of an onboard Li-Ion battery sustains about 20 min of untethered operation. Through swimming tests, we determined that the VLEIBot⁺⁺ can locomote in open loop at speeds of up to 18.7 mm/s (0.46 Bl/s) while operating its actuators at 1 Hz. We presented a study of the power-consumption requirements of a bare SMA-based microactuator of the type used to drive the VLEIBot⁺⁺ while operating in both air and water; we determined that the average power required to function underwater increases by about 1900% with respect to that required for in-air operation. These results prompted us to develop a new 13-mg low-power HWD SMA-based actuator for underwater operation that consumes an average power on the order of 80 mW when operating in air or water. This figure represents a decrease of about 91% in underwater power consumption with respect to that of the tested bare SMA-based microactuator. As part of our research program, we will integrate the new underwater SMA-based actuation technology presented here into swimmers of the VLEIBot⁺⁺ type to create the very first insect-scale AUVs.

Acknowledgments. This work was partially funded by the Washington State University (WSU) Foundation and the Palouse Club through a Cougar Cage Award to N.O.P.-A., the US National Science Foundation (NSF) through Award 2244082, and the Morgan Family Charitable Trust through a direct gift to N.O.P.-A.; additional funding was provided by the WSU Voiland College of Engineering and Architecture through a start-up fund to N.O.P.-A.

References

1. C.K. Trygstad, X.-T. Nguyen, and N. O. Pérez-Arancibia, “A New 1-mg Fast Unimorph SMA-Based Actuator for Microrobotics,” in *Proc. IEEE/RSJ Int. Conf. Intell. Robots Syst. (IROS)*, Detroit, MI, USA, Oct. 2023, pp. 2693–2700.

2. E. K. Blankenship, C. K. Trygstad, F. M. F. R. Gonçalves, and N. O. Pérez-Arancibia, "VLEIBot: A New 45-mg Swimming Microrobot Driven by a Bioinspired Anguilliform Propulsor," in *Proc. IEEE Int. Conf. Robot. Autom. (ICRA)*, Yokohama, Japan, May 2024, pp. 6014–6021.
3. C. K. Trygstad, E. K. Blankenship, and N. O. Pérez-Arancibia, "A New 10-mg SMA-Based Fast Bimorph Actuator for Microrobotics," in *Proc. IEEE/RSJ Int. Conf. Intell. Robots Syst. (IROS)*, Abu Dhabi, UAE, Oct. 2024, pp. 1349–1356.
4. K. Li, X. Zhou, Y. Liu, J. Sun, X. Tian, H. Zheng, L. Zhang, J. Deng, J. Liu, W. Chen, and J. Zhao, "A 5 cm-Scale Piezoelectric Jetting Agile Underwater Robot," *Adv. Intell. Syst.*, vol. 5, no. 4, Apr. 2023, Art. no. 2200262.
5. X. Yang, Y. Chen, L. Chang, A. A. Calderón, and N. O. Pérez-Arancibia, "Bee⁺: A 95-mg Four-Winged Insect-Scale Flying Robot Driven by Twinned Unimorph Actuators," *IEEE Robot. Automat. Lett.*, vol. 4, no. 4, pp. 4270–4277, Oct. 2019.
6. R. M. Bena, X. Yang, A. A. Calderón, and N. O. Pérez-Arancibia, "High-Performance Six-DOF Flight Control of the Bee⁺⁺: An Inclined-Stroke-Plane Approach," *IEEE Trans. Robot.*, vol. 39, no. 2, pp. 1668–1684, Apr. 2023.
7. Z. Ren, S. Kim, X. Ji, W. Zhu, F. Niroui, J. Kong, and Y. Chen, "A High-Lift Micro-Aerial-Robot Powered by Low-Voltage and Long-Endurance Dielectric Elastomer Actuators," *Adv. Mat.*, vol. 34, no. 7, Feb. 2022, Art. no. 2106757.
8. Y. Wu, J. K. Yim, J. Liang, Z. Shao, M. Qi, J. Zhong, Z. Luo, X. Yan, M. Zhang, X. Wang, R. S. Fearing, R. J. Full, and L. Lin, "Insect-Scale Fast Moving and Ultrarobust Soft Robot," *Sci. Robot.*, vol. 4, no. 32, Jul. 2019, Art. no. eaax1594.
9. W. Zhou and N. Gravish, "Soft Microrobotic Transmissions Enable Rapid Ground-Based Locomotion," in *Proc. IEEE/RSJ Int. Conf. Intell. Robots Syst. (IROS)*, Las Vegas, NV, USA, Oct. 2020, pp. 7874–7880.
10. X.-T. Nguyen, A. A. Calderón, A. Rigo, J. Z. Ge, and N. O. Pérez-Arancibia, "SMALLBug: A 30-mg Crawling Robot Driven by a High-Frequency Flexible SMA Microactuator," *IEEE Robot. Automat. Lett.*, vol. 5, no. 4, pp. 6796–6803, Oct. 2020.
11. R. M. Bena, X.-T. Nguyen, A. A. Calderón, and N. O. Pérez-Arancibia, "SMARTI: A 60-mg Steerable Robot Driven by High-Frequency Shape-Memory Alloy Actuation," *IEEE Robot. Automat. Lett.*, vol. 6, no. 4, pp. 8173–8180, Oct. 2021.
12. Y. Chen, H. Wang, E. F. Helbling, N. T. Jafferis, R. Zufferey, A. Ong, K. Ma, N. Gravish, P. Chirarattananonand, M. Kovac, and R. J. Wood, "A Biologically Inspired, Flapping-Wing, Hybrid Aerial-Aquatic Microrobot," *Sci. Robot.*, vol. 2, no. 11, Oct. 2017, Art. no. eaao5619.
13. T. Xu, G. Hwang, N. Andreff, and S. Régnier, "The Rotational Propulsion Characteristics of Scaled-Up Helical Microswimmers With Different Heads and Magnetic Positioning," in *Proc. IEEE/ASME Int. Conf. Adv. Intell. Mechatron. (AIM)*, Wollongong, NSW, Australia, Jul. 2013, pp. 1114–1120.
14. L. Zhang, T. Petit, Y. Lu, B. E. Kratochvil, K. E. Peyer, R. Pei, J. Lou, and B. J. Nelson, "Controlled Propulsion and Cargo Transport of Rotating Nickle Nanowires Near a Patterned Solid Surface," *ACS Nano*, vol. 4, no. 10, pp. 6228–6234, Sep. 2010.
15. W. Liu, X. Jia, F. Wang, and Z. Jia, "An In-Pipe Wireless Swimming Microrobot Driven by Giant Magnetostrictive Film," *Sens. Actuators A: Phys.*, vol. 160, no. 2, pp. 101–108, May 2010.
16. B. Goldberg, R. Zufferey, N. Doshi, E. F. Helbling, G. Whittredge, M. Kovac, and R. J. Wood, "Power and Control Autonomy for High-Speed Locomotion With an Insect-Scale Legged Robot," *IEEE Robot. Automat. Lett.*, vol. 3, no. 2, pp. 987–993, Apr. 2018.

17. K. Johnson, Z. Englehardt, V. Arroyos, D. Yin, S. Patel, and V. Iyer, "MilliMobile: An Autonomous Battery-Free Wireless Microrobot," in *Proc. 29th Annu. Int. Conf. Mob. Comput. Netw. (MOBICOM)*, Madrid, Spain, Oct. 2023, pp. 1360–1375.
18. X. Ji, X. Liu, V. Cacucciolo, M. Imboden, Y. Civet, A. E. Haitami, S. Cantin, Y. Perriard, and H. Shea, "An Autonomous Untethered Fast Soft Robotic Insect Driven by Low-Voltage Dielectric Elastomer Actuators," *Sci. Robot.*, vol. 4, no. 37, Dec. 2019, Art. no. eaaz6451.
19. X. Yang, L. Chang, and N. O. Pérez-Arancibia, "An 88-Milligram Insect-Scale Autonomous Crawling Robot Driven by a Catalytic Artificial Muscle," *Sci. Robot.*, vol. 5, no. 45, Aug. 2020, Art. no. eaba0015.
20. P. Spino and D. Rus, "Towards Centimeter-Scale Underwater Mobile Robots: An Architecture for Capable μ AUVs," in *Proc. IEEE Int. Conf. Robot. Autom. (ICRA)*, Yokohama, Japan, May 2024, pp. 1484–1490.
21. F. Berlinger, M. Gauci, and R. Nagpal, "Implicit Coordination for 3D Underwater Collective Behaviors in a Fish-Inspired Robot Swarm," *Sci. Robot.*, vol. 6, no. 50, Jan. 2021, Art. no. eabd8668.
22. F. Berlinger, M. Duduta, H. Gloria, D. Clarke, R. Nagpal, and R. Wood, "A Modular Dielectric Elastomer Actuator to Drive Miniature Autonomous Underwater Vehicles," in *Proc. IEEE Int. Conf. Robot. Autom. (ICRA)*, Brisbane, Australia, May 2018, pp. 3429–3435.
23. F. Berlinger, M. Saadat, H. Haj-Hariri, G. V. Lauder, and R. Nagpal, "Fish-Like Three-Dimensional Swimming With an Autonomous, Multi-Fin, and Biomimetic Robot," *Bioinspir. Biomim.*, vol. 16, no. 2, Mar. 2021, Art. no. 026018.
24. Z. Li, Y. Zhang, S. He, X. Zhu, T. Wei, and C. Hu, "Centimeter-Scale Submarine Robot for Monitoring Coral Reef Ecosystem," in *Proc. IEEE Int. Conf. Mechatron. Autom. (ICMA)*, Tianjin, China, Aug. 2024, pp. 345–350.
25. L. Cen and A. Erturk, "Bio-Inspired Aquatic Robotics by Untethered Piezohydroelastic Actuation," *Bioinspir. Biomim.*, vol. 8, no. 1, Mar. 2013, Art. no. 016006.
26. T. Wang, H. Joo, S. Song, W. Hu, C. Keplinger, and M. Sitti, "A Versatile Jellyfish-Like Robotic Platform for Effective Underwater Propulsion and Manipulation," *Sci. Adv.*, vol. 9, no. 15, p. Art. no. eadg0292, Apr. 2023.
27. F. Giorgio-Serchi, A. Arienti, and C. Laschi, "Biomimetic Vortex Propulsion: Toward the New Paradigm of Soft Unmanned Underwater Vehicles," *IEEE/ASME Trans. Mechatron.*, vol. 18, no. 2, pp. 484–493, Apr. 2013.
28. A. Villanueva, S. Bresser, S. Chung, Y. Tadesse, and S. Priya, "Jellyfish Inspired Unmanned Underwater Vehicle," in *Proc. Electroactive Polym. Actuators Devices (EAPAD)*, San Diego, CA, USA, Apr. 2009, Art. no. 72871G.
29. E. M. Purcell, "Life at Low Reynolds Number," *Amer. J. Phys.*, vol. 45, no. 1, pp. 3–11, Jan. 1977.
30. Y. A. Çengel and A. J. Ghajar, *Heat and Mass Transfer*. New York, NY, USA: McGraw-Hill Education, 2015.